CONSISTENT HYBRID DIFFUSION-TRANSPORT SPATIAL HOMOGENIZATION METHOD

A Thesis
Presented to
The Academic Faculty

by

Gabriel A. Kooreman

In Partial Fulfillment
of the Requirements for the Degree
Master of Science in Nuclear Engineering in the
Nuclear and Radiological Engineering and Medical Physics Program,
George W. Woodruff School of Mechanical Engineering

Georgia Institute of Technology
December 2013

CONSISTENT HYBRID DIFFUSION-TRANSPORT SPATIAL HOMOGENIZATION METHOD

Approved by:

Dr. Farzad Rahnema, Advisor
Nuclear and Radiological Engineering and
Medical Physics Program,
George W. Woodruff School of Mechanical
Engineering
Georgia Institute of Technology

Dr. Bojan Petrovic
Nuclear and Radiological Engineering and
Medical Physics Program,
George W. Woodruff School of Mechanical
Engineering
Georgia Institute of Technology

Dr. Dingkang Zhang
Nuclear and Radiological Engineering and
Medical Physics Program,
George W. Woodruff School of Mechanical
Engineering
Georgia Institute of Technology

Date Approved: November 4, 2013

ACKNOWLEDGEMENTS

TABLE OF CONTENTS

LIST OF TABLES

LIST OF FIGURES

SUMMARY

Recent work by Yasseri and Rahnema has introduced a consistent spatial homogenization (CSH) method completely in transport theory. The CSH method can very accurately reproduce the heterogeneous flux shape and eigenvalue of a reactor, but at high computational cost. Other recent works for homogenization in diffusion or quasi-diffusion theory are accurate for problems with low heterogeneity, such as PWRs, but are not proven for more heterogeneous reactors such as BWRs or GCRs.

To address these issues, a consistent hybrid diffusion-transport spatial homogenization (CHSH) method is developed as an extension of the CSH method that uses conventional flux weighted homogenized cross sections to calculate the heterogeneous solution. The whole-core homogenized transport calculation step of the CSH method has been replaced with a whole-core homogenized diffusion calculation. A whole-core diffusion calculation is a reasonable replacement for transport because the homogenization procedure tends to smear out transport effects at the core level. The CHSH solution procedure is to solve a core-level homogenized diffusion equation with the auxiliary source term and then to apply an on-the-fly transport-based re-homogenization at the assembly level to correct the homogenized and auxiliary cross sections. The method has been derived in general geometry with continuous energy, and it is implemented and tested in fine group, 1-D slab geometry on controlled and uncontrolled BWR and HTTR benchmark problems. The method converges to within 2% mean relative error for all four configurations tested and has computational efficiency 2 to 4 times faster than the reference calculation.

CHAPTER I

INTRODUCTION

Recently, Yasseri and Rahnema [13] developed a new consistent spatial homogenization method (CSH) using only transport theory. The key feature of the CSH method is the introduction of an auxiliary cross section to homogenize without reducing the phase space of the problem. The advantage of CSH is that the homogenization can very accurately reproduce the heterogeneous flux shape and eigenvalue of a reactor core while increasing computational efficiency slightly with a correct choice of convergence criteria. However, the CSH method requires multiple transport calculations, making it a computationally slower homogenization than many nodal diffusion methods. This work extends the CSH method to diffusion theory, resulting in a hybrid diffusion-transport homogenization method that can reproduce the heterogeneous flux shape in less time than the CSH method.

Several recent techniques for homogenization within diffusion or quasi-diffusion have been developed which focus on reproducing heterogeneous eigenvalue and reaction rates, but do not focus on reproducing the heterogeneous flux profile [1, 4, 6, 8, 10]. For this reason, many of these works do not report flux errors, but instead report reaction rates and average flux over each homogenized region. These averages are often very accurate but are not a good estimate of local flux or pin powers. Additionally, some of these methods perform simultaneous homogenization with energy condensation, which can lead to error cancellation in the average flux, but increased error in calculations of local effects.

Homogenization of the diffusion equation with discontinuity factors has long been an accepted homogenization method. Recently Sanchez [10] introduced a method of applying both current discontinuity factors (CDFs) and flux discontinuity factors (FDFs) to achieve more accurate homogenizations. In Sanchez's method, the FDFs are a generalization of Smith's discontinuity factors (DFs) homogenization [12]. Sanchez's method achieves similar results to Smith's DFs but with better precision in reactors where transport effects dominate. Like

other recent homogenization techniques in diffusion theory, these discontinuity factor methods do not naturally re-homogenize and so cannot reproduce local effects, such as pin powers. Since discontinuity factors are a common and accepted method for homogenization, the core calculation results of this work are compared to homogenizations of the same cores using discontinuity factors.

The Consistent Hybrid Spatial Homogenization (CHSH) method involves iterations between assembly-level transport calculations and whole-core diffusion calculations. Other hybrid diffusion-transport iterative methods have been developed with a similar procedure. One recent method by Roberts *et. al.* [9] was developed for the analysis of LWR cores. The Iterative Transport-Diffusion Method (ITDM) developed by Roberts *et. al.* is similar to the CHSH method in that it iterates between whole-core diffusion and assembly-level transport, but one key difference is that the ITDM uses nodal diffusion rather than fine-mesh diffusion at the core level. Additionally, the ITDM is not yet shown to work for fast reactors.

In this work, the CSH method introduced by Yasseri and Rahnema is extended to diffusion theory, resulting in a hybrid homogenization method. The method is derived in general geometry and continuous energy in Chapter 2, and has been implemented in 1-D and tested using 1-D BWR and HTTR benchmark problems. The details of its 1-D implementation are found in Chapter 3, and the results of the whole core tests are found in Chapter 4. The method has been compared against both discontinuity factor homogenization and heterogeneous S-8 reference solutions in order to test for accuracy and efficiency. Concluding remarks and notes about future work are provided in Chapter 5.

<center>**CHAPTER II**</center>

<center>**METHOD**</center>

2.1   Spatial homogenization in transport theory

The CHSH method is derived using Yasseri and Rahnema's Consistent Spatial Homogenization
(CSH) method as a starting point. For the sake of completeness, a summary of the derivation
of the CSH method is provided below [13]. The fine-mesh heterogeneous angular flux within
a homogenized region V^h with isotropic fission and a scattering kernel dependent on the
scattering angle cosine $\mu_0 = \hat{\Omega} \cdot \hat{\Omega}'$ is governed by

$$
\begin{aligned}
\hat{\Omega} \cdot \nabla \psi(\vec{r}, E, \hat{\Omega}) &+ \sigma(\vec{r}, E) \psi(\vec{r}, E, \hat{\Omega}) \\
&= \int_{4\pi} \mathrm{d}\hat{\Omega}' \int \mathrm{d}E' \sigma_s(\vec{r}, E' \to E, \hat{\Omega} \cdot \hat{\Omega}') \psi(\vec{r}, E', \hat{\Omega}) \\
&+ \frac{\chi(E)}{4\pi k} \int_{4\pi} \mathrm{d}\hat{\Omega}' \int \mathrm{d}E' \nu \sigma_f(\vec{r}, E') \psi(\vec{r}, E', \hat{\Omega}') \\
&\forall \vec{r} \in V^h
\end{aligned}
\tag{1}
$$

The basis of the CSH method[13] is that the fine mesh solution can be obtained from a
homogenized equation with an auxiliary source term, as in Eq. (2).

$$
\begin{aligned}
\hat{\Omega} \cdot \nabla \psi^h(\vec{r}, E, \hat{\Omega}) &+ \sigma^h(E) \psi^h(\vec{r}, E, \hat{\Omega}) \\
&= \int_{4\pi} \mathrm{d}\hat{\Omega}' \int \mathrm{d}E' \sigma_s^h(E' \to E, \hat{\Omega} \cdot \hat{\Omega}') \psi^h(\vec{r}, E', \hat{\Omega}') \\
&+ \frac{\chi(E)}{4\pi k^h} \int_{4\pi} \mathrm{d}\hat{\Omega}' \int \mathrm{d}E' \nu \sigma_f^h(E') \psi^h(\vec{r}, E', \hat{\Omega}') \\
&+ \sigma_{\text{aux}}(\vec{r}, E, \hat{\Omega}) \phi_{\text{avg}}^h(E); \quad \forall \vec{r} \in V^h
\end{aligned}
\tag{2}
$$

Here, the superscript 'h' refers to homogenized values. Note that the cross sections within
the homogenized region are no longer functions of $\vec{r}$. The symbol ϕ_{avg}^h represents the average
scalar flux in the homogenized region V^h. In order to preserve the heterogeneous solution and

<center>3</center>

the heterogeneous eigenvalue, σ_{aux} must be defined as follows,

$$
\begin{aligned}
\sigma_{\mathrm{aux}} = \frac{1}{\phi_{\mathrm{avg}}(E)} &\left[\int_{4\pi} \mathrm{d}\hat{\Omega}' \int \mathrm{d}E' \Delta\sigma_s(\vec{r}, E' \to E, \hat{\Omega}\cdot\hat{\Omega}')\psi(\vec{r}, E', \hat{\Omega}') \right. \\
&+ \frac{1}{4\pi k} \int_{4\pi} \mathrm{d}\hat{\Omega}' \int \mathrm{d}E' \chi(E)\Delta\nu\sigma_f(\vec{r}, E')\psi(\vec{r}, E', \hat{\Omega}') \\
&\left. - \Delta\sigma(\vec{r}, E)\psi(\vec{r}, E, \hat{\Omega}) \right]
\end{aligned}
\tag{3}
$$

where,

$$
\Delta\sigma_{t,s,f}(\vec{r}) = \sigma_{t,s,f}(\vec{r}) - \sigma_{t,s,f}^h
\tag{4}
$$

Yasseri and Rahnema[13] then expand σ_{aux} into spatial and angular components. Spherical harmonics are used in the angular domain, while any set of orthogonal basis functions $G_p(\vec{r})$ with weighting function $w(\vec{r})$ and factor a_p can be used for the spatial domain. The auxiliary cross section becomes

$$
\begin{aligned}
\sigma_{\mathrm{aux}}(\vec{r}, E, \hat{\Omega}) &= \sum_{\ell=0}^{L} \sum_{m=-\ell}^{\ell} \sum_{p=0}^{P} \frac{Y_{\ell m}(\hat{\Omega})}{4\pi} a_p G_p(\vec{r}) \sigma_{\mathrm{aux}}^{\ell m, p}(E) \\
&= \sum_{\ell=0}^{L} \sum_{m=-\ell}^{\ell} \sum_{p=0}^{P} \frac{Y_{\ell m}(\hat{\Omega})}{4\pi} a_p G_p(\vec{r}) [\alpha_{\ell m, p}(E) + \beta_{\ell m, p}(E) - \gamma_{\ell m, p}(E)]
\end{aligned}
\tag{5}
$$

Where α, β and γ are defined in Eqs. (6) to (8)

$$
\alpha_{\ell m, p}(E) = \frac{1}{\phi_{\mathrm{avg}}^h(E)} \int_{4\pi} \mathrm{d}\hat{\Omega}' \int_{4\pi} \mathrm{d}\hat{\Omega} \int \mathrm{d}E' \int_{V^h} \mathrm{d}\vec{r} w(\vec{r}) G_p(\vec{r}) Y_{\ell m}^*(\hat{\Omega}) \Delta\sigma_s(\vec{r}, E' \to E, \hat{\Omega}\cdot\hat{\Omega}')\psi(\vec{r}, E', \hat{\Omega}')
$$

$$
\tag{6}
$$

$$
\beta_{\ell m, p}(E) = \frac{1}{4\pi k} \frac{1}{\phi_{\mathrm{avg}}^h(E)} \int_{4\pi} \mathrm{d}\hat{\Omega}' \int_{4\pi} \mathrm{d}\hat{\Omega} \int \mathrm{d}E' \int_{V^h} \mathrm{d}\vec{r} w(\vec{r}) G_p(\vec{r}) Y_{\ell m}^*(\hat{\Omega}) \chi(E)\Delta\nu\sigma_f(\vec{r}, E')\psi(\vec{r}, E', \hat{\Omega}')
$$

$$
\tag{7}
$$

$$
\gamma_{\ell m, p}(E) = \frac{1}{\phi_{\mathrm{avg}}^h(E)} \int_{4\pi} \mathrm{d}\hat{\Omega} \int_{V^h} \mathrm{d}\vec{r} w(\vec{r}) G_p(\vec{r}) Y_{\ell m}^*(\hat{\Omega}) \Delta\sigma(\vec{r}, E)\psi(\vec{r}, E, \hat{\Omega})
\tag{8}
$$

where

$$
\phi_{\mathrm{avg}}(E) = a_0 \int_{V^h} \mathrm{d}\vec{r} \int_{4\pi} \mathrm{d}\hat{\Omega} w(\vec{r}) G_0(\vec{r}) \psi(\vec{r}, E, \hat{\Omega})
\tag{9}
$$

2.2 Spatial homogenization in diffusion theory

The CSH method can be modified to use a low angular order, such as in diffusion theory. Transport effects for the homogenized equation will tend to be less pronounced, as the

4

homogenization will tend to smear out troublesome local effects. Implementation of a transport based re-homogenization can correct for these transport effects in the solution.

If the scattering kernel in Eq. (2) is assumed to be linearly anisotropic, the equation becomes

$$
\begin{aligned}
\hat{\Omega} \cdot \nabla \psi^h(\vec{r}, E, \hat{\Omega}) &+ \sigma^h(E)\psi^h(\vec{r}, E, \hat{\Omega}) \\
&= \int_{4\pi} d\hat{\Omega}' \int dE' \frac{1}{4\pi} \left(\sigma_{s0}^h(E' \to E) + 3\hat{\Omega} \cdot \hat{\Omega}' \sigma_{s1}^h(E' \to E) \right) \psi^h(\vec{r}, E', \hat{\Omega}') \\
&\quad + \frac{\chi(E)}{4\pi k^h} \int_{4\pi} d\hat{\Omega}' \int dE' \nu \sigma_f^h(E') \psi^h(\vec{r}, E', \hat{\Omega}') \\
&\quad + \sigma_{\text{aux}}(\vec{r}, E, \hat{\Omega}) \phi_{\text{avg}}^h(E); \quad \forall \vec{r} \in V^h
\end{aligned}
\tag{10}
$$

where σ_{s0}^h and σ_{s1}^h are the homogenized zeroth and first order expansions of the scattering kernel in Legendre polynomials of $\hat{\Omega} \cdot \hat{\Omega}'$. Taking the 0th and 1st angular moments of Eq. (10) results in Eqs. (11) and (12).

$$
\begin{aligned}
\nabla \cdot J^h(\vec{r}, E) &+ \sigma^h(E)\phi^h(\vec{r}, E) \\
&= \int dE' \sigma_{s0}^h(E' \to E)\phi^h(\vec{r}, E') + \frac{\chi(E)}{k^h} \int dE' \nu \sigma_f^h(E')\phi^h + \sigma_{\text{aux}}^0(\vec{r}, E)\phi_{\text{avg}}^h(E)
\end{aligned}
\tag{11}
$$

$$
\nabla \cdot \Pi^h(\vec{r}, E) + \sigma_{tr}^h(E)J(\vec{r}, E) = \vec{\sigma}_{\text{aux}}^1(\vec{r}, E)\phi_{\text{avg}}^h
\tag{12}
$$

Where $\sigma_{\text{aux}}^0(\vec{r}, E)$ and $\vec{\sigma}_{\text{aux}}^1(\vec{r}, E)$ are defined in Eqs. (13) and (14) as the zeroth and first angular moments of $\sigma_{\text{aux}}(\vec{r}, E, \hat{\Omega})$, $\Pi^h(\vec{r}, E)$ is defined in Eq. (15), and $\sigma_{tr}^h(E)$ is defined in Eq. (16)

$$
\sigma_{\text{aux}}^0(\vec{r}, E) = \int_{4\pi} d\hat{\Omega} \sigma_{\text{aux}}(\vec{r}, E, \hat{\Omega})
\tag{13}
$$

$$
\vec{\sigma}_{\text{aux}}^1(\vec{r}, E) = \int_{4\pi} d\hat{\Omega} \sigma_{\text{aux}}(\vec{r}, E, \hat{\Omega})\hat{\Omega}
\tag{14}
$$

$$
\Pi^h(\vec{r}, E) = \int_{4\pi} d\hat{\Omega}\hat{\Omega}\hat{\Omega}\psi^h(\vec{r}, E, \hat{\Omega})
\tag{15}
$$

$$
\sigma_{tr}^h(E) = \frac{\int dE' J(E')\sigma_{s1}^h(E' \to E)}{J(E)\sigma_{s1}^h(E)}J(E)\sigma_{s1}^h(E)
\tag{16}
$$

if the balance principle ($\int dE' J(E')\sigma_{s1}^h(E' \to E) = J(E)\int dE' \sigma_{s1}^h(E \to E')$) is applied, then Eq. (16) becomes the usual definition of the transport cross section.

Substituting Eq. (12) into Eq. (11) and making the P-1 approximation $\left(\nabla \cdot \Pi^h(\vec{r},E) = \frac{1}{3}\nabla\phi^h(\vec{r},E)\right)$ results in a single homogenized diffusion equation. Note that σ_{aux}^1 is a vector quantity.

$$
\begin{aligned}
-D^h(E)&\nabla^2\phi^h(\vec{r},E) + \sigma^h(E)\phi^h(\vec{r},E) \\
&= \int dE' \left[\sigma_{s0}^h(E' \to E)\phi^h(\vec{r},E') + \frac{\chi(E)}{k^h}\nu\sigma_f^h(E')\phi^h(\vec{r},E') \right] \\
&+ \phi_{\text{avg}}^h \left(\sigma_{\text{aux}}^0(\vec{r},E) - \frac{\nabla \cdot \vec{\sigma}_{\text{aux}}^1(\vec{r},E)}{\sigma_{tr}^h(E)} \right)
\end{aligned}
\tag{17}
$$

In practice it is more convenient to discretize and use Eqs. (11) and (12) than Eq. (17). Using Eq. (17) limits the possible discretizations that can be used in the solution. The spatial discretizations of Eqs. (11) and (12) that is used in this paper will be discussed in Section 3.1.

The generalized albedo boundary conditions developed for quasi-diffusion[1] can be used as boundary conditions for the homogenized diffusion equation,

$$
J^h(\vec{r}_s,E) \cdot \hat{n}_s = \frac{1 - \lambda_1(E)}{1 + \lambda_0(E)}C_{r_s}(E)\phi^h(\vec{r}_s,E)
\tag{18}
$$

$$
\lambda_n(E) = \frac{\int_{2\pi^-} d\hat{\Omega} |\hat{n}_s \cdot \hat{\Omega}|^n \psi(\vec{r}_s,\hat{\Omega},E)}{\int_{2\pi^+} d\hat{\Omega} (\hat{n}_s \cdot \hat{\Omega})^n \psi(\vec{r}_s,\hat{\Omega},E)}
\tag{19}
$$

$$
C_{r_s}(E) = \frac{\int_{2\pi^-} d\hat{\Omega} (\hat{n}_s \cdot \hat{\Omega}) \psi(\vec{r}_s,\hat{\Omega},E)}{\int_{2\pi^+} d\hat{\Omega} \psi(\vec{r}_s,\hat{\Omega},E)}
\tag{20}
$$

2.3 Solution procedure

Because the definition of σ_{aux} relies on *a priori* knowledge of the heterogeneous flux, it is necessary to iterate and apply transport re-homogenization in order to obtain an approximation for σ_{aux}. Extra care must be taken to reconcile the diffusion-based core calculation with the transport assembly calculations used in re-homogenization. The procedure for solving a core eigenvalue problem with the CHSH method is as follows:

1. Perform heterogeneous calculations at the assembly level with approximate boundary conditions (such as specular reflective), and generate initial homogenized and auxiliary cross sections for each assembly.

2. Solve the homogeneous whole-core diffusion equation using the homogenized cross sections and the added σ_{aux} source term in each region.

3. Expand the core level incoming flux at the surface of each assembly. Two methods are proposed and implemented in this paper to expand the incoming fluxes for each assembly, the diffusion approximation method (DA) and the current iteration method (CI). The DA method uses a diffusion approximation from the whole core calculation at each assembly surface as in Eq. (21).

$$\psi(\vec{r}_{\text{surf}}, E, \hat{\Omega}) \approx \frac{1}{4\pi} \left(\phi^h(\vec{r}_{\text{surf}}, E) + 3\hat{\Omega} \cdot \vec{J}^h(\vec{r}_{\text{surf}}, E) \right) \tag{21}$$

The CI method adapts the previous iteration's surface flux by weighting it with the change in surface current calculated by the core solver,

$$\psi^{(n+1/2)}(\vec{r}_{\text{surf}}, E, \hat{\Omega}) \approx \psi^{(n)}(\vec{r}_{\text{surf}}, E, \hat{\Omega}) \frac{J_{\text{inc}}^{(n+1/2),h}(\vec{r}_{\text{surf}}, E)}{J_{\text{inc}}^{(n)}(\vec{r}_{\text{surf}}, E)} \tag{22}$$

The superscript n refers to the iteration number. Half-integer iterations are the results from core-level calculation, while whole-integer iterations are the results from assembly level calculations. J_{inc} refers to the incoming current for each assembly surface and can be defined by $J_{\text{inc}}(\vec{r}_{\text{surf}}, E) = -\vec{n} \cdot J(\vec{r}_{\text{surf}}, E)$, where $\vec{n}$ is the unit surface normal. The major advantage of this method is that it preserves the transport angular flux distribution (I.e., it does not require the angular flux at the surface to be linearly anisotropic). The DA and CI methods do not preclude each other's use and can, in fact, be used interchangeably within a calculation.

4. Perform heterogeneous fixed source calculations at the assembly level with the core eigenvalue from Step 2 and the incoming fluxes calculated in Step 3

5. Repeat Steps 2 to 4 until the flux and eigenvalue meet the convergence criteria defined in Eqs. (23) and (24), where n is the iteration number as used in Eq. (22). Note that the eigenvalue is calculated in the core solver step (half-integer iteration number), and the average flux comes from the de-homogenized flux (integer iteration number).

$$\left| \frac{\phi_{\text{avg}}^{h,n}(\vec{r}, E) - \phi_{\text{avg}}^{h,n-1}(\vec{r}, E)}{\phi_{\text{avg}}^{h,n}(\vec{r}, E)} \right|_{\text{max}} < \epsilon_\phi \tag{23}$$

$$\left| \frac{k^{h,n-1/2} - k^{h,n-3/2}}{k^{h,n-1/2}} \right| < \epsilon_k \tag{24}$$

CHAPTER III

IMPLEMENTATION IN 1D

The CHSH method has been derived for the general case. For verification purposes, the method has been implemented in 1-D. In the interest of simplicity, it is assumed that the scattering kernel is isotropic and cross sections have been transport-corrected. The multigroup approximation is used to discretize the energy variable.

3.1 1-D discretization

Let us define the following mesh on each homogenized region, $\{x_{i-1/2}, i = 1, ..., N+1\}$, where N is the number of meshes in a homogenized region. The width of the ith mesh is $h_i = x_{i+1/2} - x_{i-1/2}$. A convenient discretization for the homogenized diffusion equation is to define ϕ_i as a mesh averaged value and to define $J_{i+1/2}$ on the mesh boundaries. This discretization will work well with the re-homogenization methods proposed in Section 2.3 because $J_{1/2}$ and $J_{N+1/2}$ are the currents on the boundaries of the region.

The central difference approximation of Eq. (11) is taken at the center of each mesh i,

$$\frac{1}{h_i}(J^g_{i+1/2} - J^g_{i-1/2}) + \sigma^{h,g}\phi^g_i = S^g_{0,i} \tag{25}$$

where,

$$S^g_{0,i} \equiv \sum_{g'}^{G} \sigma^h_{s0}(g' \to g)\tilde{\phi}^{g'}_i + \frac{\chi^g}{k^h}\sum_{g'}^{G} \nu\sigma^{h,g'}_f \tilde{\phi}^{g'}_i + \sigma^g_{\text{aux},0,i}\tilde{\phi}^{h,g}_{\text{avg}} \tag{26}$$

Some care must be taken to discretize the equation at the interface between meshes, because some mesh interfaces may be located between two different homogenized regions. For this reason, it is necessary to discretize Eq. (12) separately for the region to the left of the interface and to the right of the interface. Two equations are derived, one by integrating from x_i to $x_{i+1/2}$ and the other by integrating from $x_{i+1/2}$ to x_{i+1},

$$\frac{2}{3h_i}(\phi^g_{i+1/2} - \phi^g_i) + \sigma^{h,g}_i J^g_{i+1/2} = S^g_{1,i} \tag{27}$$

and

$$\frac{2}{3h_{i+1}}(\phi_{i+1}^g - \phi_{i+1/2}^g) + \sigma_{i+1}^{h,g} J_{i+1/2}^g = S_{1,i+1}^g \tag{28}$$

where,

$$S_{1,i}^g \equiv \sigma_{\text{aux},1,i}^g \tilde{\phi}_{\text{avg},i}^{h,g} \tag{29}$$

where the tildes indicate that the value from the last iteration is to be used (as is traditional in numerical solutions of the diffusion equation), and where $\tilde{\phi}_{\text{avg}}^{h,g}$ is taken from the appropriate homogenized region. Note that in Eqs. (27) and (28) the homogenized cross sections have been given an index i. This is because regions i and $i+1$ may lie in two different homogenized regions. Within one homogenized region σ_i and σ_{i+1} will always be identical.

Eqs. (27) and (28) can be solved for $\phi_{i+1/2}$ and $J_{i+1/2}$ to obtain,

$$\phi_{i+1/2}^g = \frac{\sigma_{i+1}^{h,g} S_{1,i}^g - \sigma_i^{h,g} S_{1,i+1} + \frac{2\sigma_{i+1}^{h,g}}{3h_i}\phi_i^g + \frac{2\sigma_i^{h,g}}{3h_{i+1}}\phi_{i+1}^g}{\frac{2\sigma_{i+1}^{h,g}}{3h_i} + \frac{2\sigma_i^{h,g}}{3h_{i+1}}} \tag{30}$$

$$J_{i+1/2}^g = \frac{\frac{1}{h_{i+1}}S_{1,i}^g + \frac{1}{h_i}S_{1,i+1}^g - \frac{2}{3h_i h_{i+1}}(\phi_{i+1}^g - \phi_i^g)}{\frac{\sigma_i^{h,g}}{h_{i+1}} + \frac{\sigma_{i+1}^{h,g}}{h_i}} \tag{31}$$

Eq. (31) can be substituted back into Eq. (25) to yield a three point formula for the mesh average flux.

The 1-D benchmark problems used by this paper have specular reflective boundary conditions along the left side and vacuum conditions on the right. Both of these conditions can be implemented by a modification to Eq. (31) at the boundary. Specular reflective boundary conditions on the left side of the reactor are taken into account simply by setting $J_{1/2}^g = 0$. Vacuum conditions ($\lambda = 0$) can be applied using Eq. (18) to obtain $J_{N+1/2}^g = C_R^g \phi_{N+1/2}$, which can be substituted into Eq. (27) resulting in the vacuum boundary condition at the right,

$$J_{N+1/2}^g = \frac{S_{1,N}^g + \frac{2}{3h_N}\phi_N^g}{\sigma_N^{h,g} + \frac{2}{3h_N C_R}} \tag{32}$$

3.2 *Choice of basis functions*

In 1D geometry, Legendre polynomials can be substituted for spherical harmonics. this means that the auxiliary cross section over a homogenized region can be defined in 1-D by the

9

following adaptation to Eq. (5),

$$\sigma_{\text{aux}}^g(x,\mu) = \frac{1}{\phi_{\text{avg}}^g} \left\{ \frac{1}{2} \sum_{g'} \left[\sigma_{s0}^{g' \to g}(x) - \sigma_{s0}^{h,g' \to g} \right] \phi^{g'}(x) \right.$$

$$+ \frac{1}{2k} \sum_{g'} \left[\chi^g \nu \sigma_f^{g'}(x) - \chi^g \nu \sigma_f^{h,g'} \right] \phi^{g'}(x) \tag{33}$$

$$\left. - \sum_{\ell'=0}^{L} \frac{2\ell'+1}{2} P_{\ell'}(\mu)[\sigma^g(x) - \sigma^{h,g}]\phi_{\ell'}^g(x) \right\}$$

If $f_n(x)$ is chosen to be an orthonormal basis function on the interval with $w(x) = 1$, then the auxiliary cross section can be further simplified to

$$\sigma_{\text{aux}}^g(x,\mu) = \sum_{\ell=0}^{L} \frac{2\ell+1}{2} P_l(\mu) \sum_{n=0}^{N} f_n(x)[\delta_{0,\ell}\alpha_n^g + \delta_{0,\ell}\beta_n^g - \gamma_{n,\ell}^g] \tag{34}$$

with

$$\alpha_n^g = \frac{\sum_{g'} \int_0^a f_n(x) \left[\Delta\sigma_{s0}^{g' \to g}(x) \right] \phi^{g'}(x)dx}{\int_0^a \phi^g(x)dx/a} \tag{35}$$

$$\beta_n^g = \frac{\sum_{g'} \int_0^a f_n(x) \left[\chi^g \Delta\nu\sigma_f^{g'}(x) \right] \phi^{g'}(x)dx}{\int_0^a \phi^g(x)dx/a} \tag{36}$$

$$\gamma_{n,\ell}^g = \frac{\int_0^a f_n(x)[\Delta\sigma^g]\phi_\ell^g(x)dx}{\int_0^a \phi^g(x)dx/a} \tag{37}$$

Some truncation error will be introduced to this approximation due to the need for a cut off of the expansion function. This makes the choice of expansion function very important for minimizing the numerical error of the auxiliary cross section and therefore the homogenization. Yasseri and Rahnema[13] chose a Fourier series expansion in space, modifying the auxiliary cross section into a periodic function over each region. A Fourier expansion was chosen in order to minimize the truncation error for a given expansion order, however Fourier series expansions suffer from Gibbs phenomenon issues near the discontinuities at the boundaries of each region.

Instead of a traditional expansion function, a linear interpolation of the auxiliary cross section is proposed from the fine mesh to the homogenized mesh. An advantage of choosing a linear interpolation is that there can never be any overshoot near boundaries in σ_{aux}. Additionally, $f_n(x)$ is evaluated in Eqs. (40) to (42) only as an integrand. Linear interpolation as an integrand evaluates to numerical integration using the trapezoidal rule, which is an accurate and consistent approximation to the true integral (with second-order error). Extra

care must be taken in order to account for the fact that this choice of $f_n(x)$ is not strictly an orthonormal basis function. For a linear interpolation, $f_n(x)$ is chosen to be piecewise defined,

$$f_n(x) = \begin{cases} \frac{x - x_{n-1}}{x_n - x_{n-1}} & x_{n-1} \leq x < x_n \\ \frac{x_{n+1} - x}{x_{n+1} - x_n} & x_n \leq x < x_{n+1} \\ 0 & \text{otherwise} \end{cases} \tag{38}$$

Under this definition, new definitions of α_n^g, β_n^g, and $\gamma_{n,\ell}^g$ are required, in order to account for the new type of spatial basis function,

$$\sigma_{\text{aux}}^g(x, \mu) =$$

$$\sum_{\ell=0}^{L} \frac{2\ell + 1}{2} P_l(\mu) \left[f_n(x)(\delta_{0,\ell} \alpha_n^g + \delta_{0,\ell} \beta_n^g - \gamma_{n,\ell}^g) + f_{n+1}(x)(\delta_{0,\ell} \alpha_{n+1}^g + \delta_{0,\ell} \beta_{n+1}^g - \gamma_{n+1,\ell}^g) \right]$$

$$x_n \leq x < x_{n+1}$$

$$\tag{39}$$

with,

$$\alpha_n^g = \frac{\sum_{g'} \int_{x_{n-1}}^{x_{n+1}} f_n(x) \left[\Delta \sigma_{s0}^{g' \to g}(x) \right] \phi^{g'}(x) dx}{\int_{x_{n-1}}^{x_{n+1}} \phi^g(x) dx / a} \tag{40}$$

$$\beta_n^g = \frac{\sum_{g'} \int_{x_{n-1}}^{x_{n+1}} f_n(x) \left[\chi^g \Delta \nu \sigma_f^{g'}(x) \right] \phi^{g'}(x) dx}{\int_{x_{n-1}}^{x_{n+1}} \phi^g(x) dx / a} \tag{41}$$

$$\gamma_{n,\ell}^g = \frac{\int_{x_{n-1}}^{x_{n+1}} f_n(x) [\Delta \sigma^g] \phi_\ell^g(x) dx}{\int_{x_{n-1}}^{x_{n+1}} \phi^g(x) dx / a} \tag{42}$$

CHAPTER IV

NUMERICAL RESULTS

4.1 1-D core problems

In this section, two different 1-D core problems are used to test the CHSH method. The procedure described in Chapter 2 is used for both reactors. For each reactor, calculations were performed using both the diffusion approximation re-homogenization and the current iteration re-homogenization. The homogenized equation is solved using the diffusion equation as described in Chapter 3, with the auxiliary cross section expanded in linear B-splines in space. Core calculations were performed using a fine mesh, 47-group diffusion solver, and re-homogenization calculations were performed using a fixed-source, 47-group S-8 transport solver with diamond difference discretization. Re-homogenization convergence criteria detailed in Eqs. (23) and (24) were chosen to be $\epsilon_\phi = 10^{-3}$ and $\epsilon_k = 10^{-4}$. The results calculated for both cores are compared to results using standard discontinuity factor diffusion homogenization.

Flux errors are reported comparing the results of the assembly fixed-source de-homogenization to the fine-mesh transport reference solution. Flux errors are reported in average, mean, and maximum relative errors, which are defined as

$$
\begin{aligned}
\mathrm{AVG}_g &= \frac{\int \mathrm{d}x |e^g(x)|}{\int \mathrm{d}x} \\
\mathrm{MRE}_g &= \frac{\int \mathrm{d}x |e^g(x)| \phi_{\mathrm{hom}}^g(x)}{\int \mathrm{d}x \phi_{\mathrm{ref}}^g} \\
\mathrm{MAX}_g &= \max(|e^g(x)|)
\end{aligned}
\tag{43}
$$

with

$$
e^g(x) = 100\% \frac{\phi_{\mathrm{ref}}^g(x) - \phi_{\mathrm{hom}}^g(x)}{\phi_{\mathrm{ref}}^g(x)}
\tag{44}
$$

Both the homogenized solver and the fine-mesh solver were discretized spatially to approximately one half of a mean free path. This does not mean that the fine mesh and homogenized

equations are on the same mesh, however, as the homogenization process necessarily changes the mean free path in each region.

4.1.1 1-D BWR core

BWR core calculations were performed on a GE9 BWR lattice[5] consisting of twelve fuel types including four 5.84% Gd fuel pins. The core was generated by modeling in half symmetry with full heterogeneity. Fuel bundles were depleted to 17 Gwd/THM for three void parameters (0%, 40%, and 70%) in 47-groups. The HELIOS[11] lattice depletion code was used to perform transport calculations on 2-D bundles and 1-D cross sections were generated using a flux-weighted transverse integration of the regions of the 2-D model. The core is composed of twenty bundles of width 15.24 cm for two different control configuration, controlled (SRI) and uncontrolled (ARO). Each bundle of the core is composed of 11 regions as depicted in Figure 1a. Bundles labeled "A" are fresh fuel, and bundles labeled "B" are depleted. The 1-D BWR benchmark problem was generated by Douglass and Rahnema, and additional details about the core can be found in Reference [2].

(a) 1-D BWR bundle layout

(b) 1-D BWR core layout for uncontrolled configuration

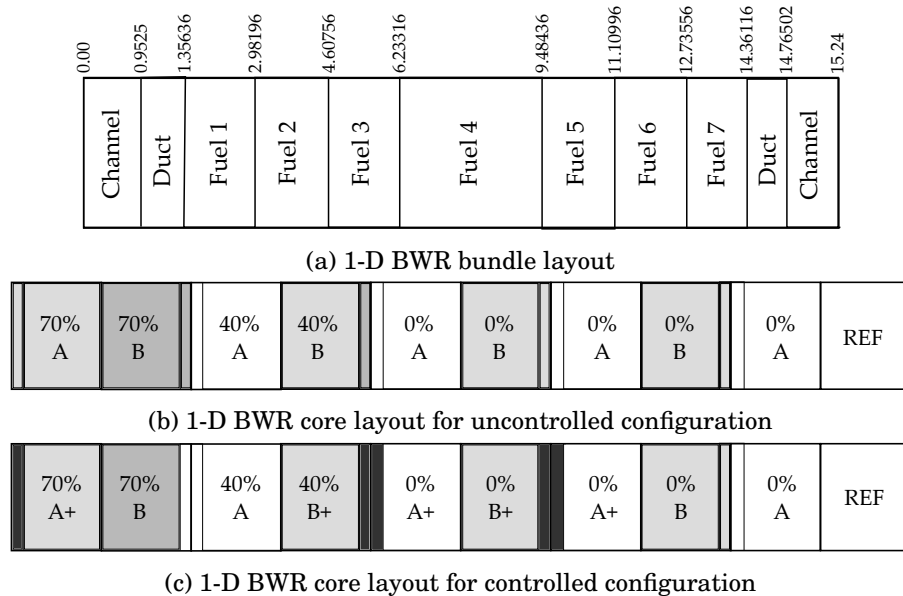(c) 1-D BWR core layout for controlled configuration

Figure 1: 1-D BWR core and bundle layouts for controlled and uncontrolled configurations. Moderator regions are composed entirely of moderator, '+' indicates the presence of a control rod, and the percentage is a depletion void parameter[2]

The reference flux calculated for the controlled and uncontrolled BWR cores can be found in Figures 2 and 3. The ARO configuration is fully uncontrolled, while the controlled configuration has some control rods in, emulating the reactor near criticality, i.e., k for the controlled case is meant to be close to 1. The reference calculation is a fully heterogeneous 47 group S-8 calculation with a diamond difference discretization scheme and half mean free path meshing, totaling about 1300 total meshes for each reactor case.

Figure 2: S-8 reference solution to the uncontrolled BWR reactor, k = 1.06795. Vertical gridlines represent assembly interfaces.

Figures 4 to 7 show the flux error results of the homogenized calculation on both cores and for both boundary condition approximations used in re-homogenization. The homogenized calculations were performed using a 47 group diffusion homogenized solver and a 47 group S-8 rehomogenization. All meshings were done to about half of a mean free path, leading to the coarse mesh solver having roughly half as many total meshes as the fine mesh solver. All four full-core trials took a total of four outer iterations in order to converge to this solution. Note that for all four cases flux errors are sharply peaked near the interfaces between homogenized regions. This suggests that the majority of the error in the calculation is coming from the approximation for the flux at the boundaries. The source of the error will be discussed in

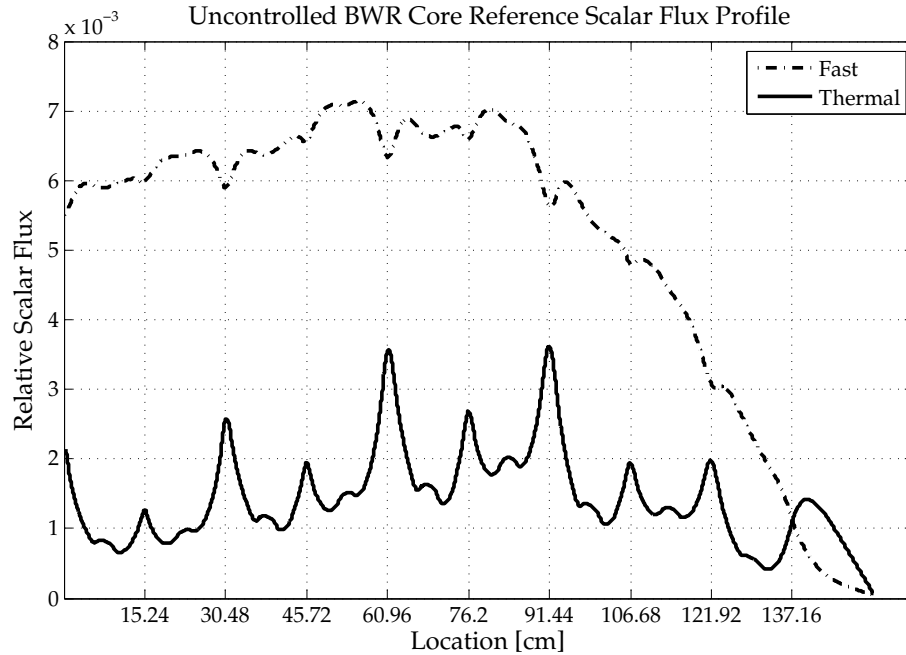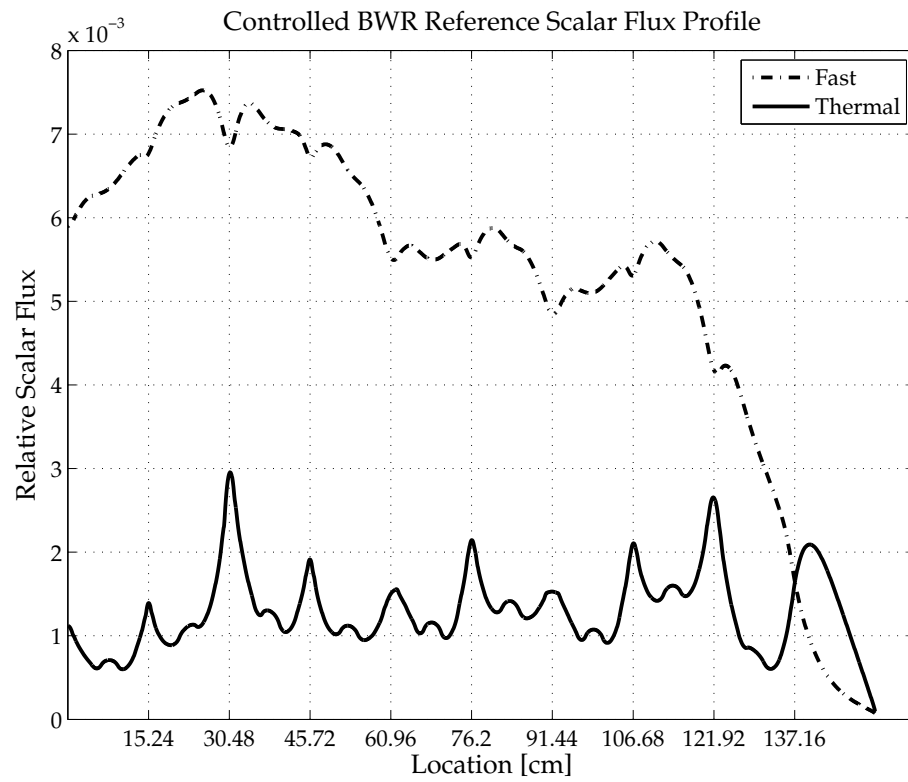Figure 3: S-8 reference solution to the controlled BWR reactor, $k = 1.00491$. Vertical gridlines represent assembly interfaces.

greater detail in Section 4.2. Note that the flux error peaks at around ±4% or lower for all four cases. The results of these calculations are tabulated in Table 6.

Of special note is the comparison between the diffusion approximation boundary conditions and the current iteration boundary conditions for the BWR. In every case, the current iteration approximation performed better in the fast spectrum. The fast spectrum for a BWR tends to have higher anisotropy, and so this indicates that the current iteration method performs better than the diffusion approximation method as anisotropy increases. However, the current iteration method performs slightly worse than the diffusion approximation method in the thermal spectrum and results in a slightly less accurate approximation for the reactor eigenvalue.
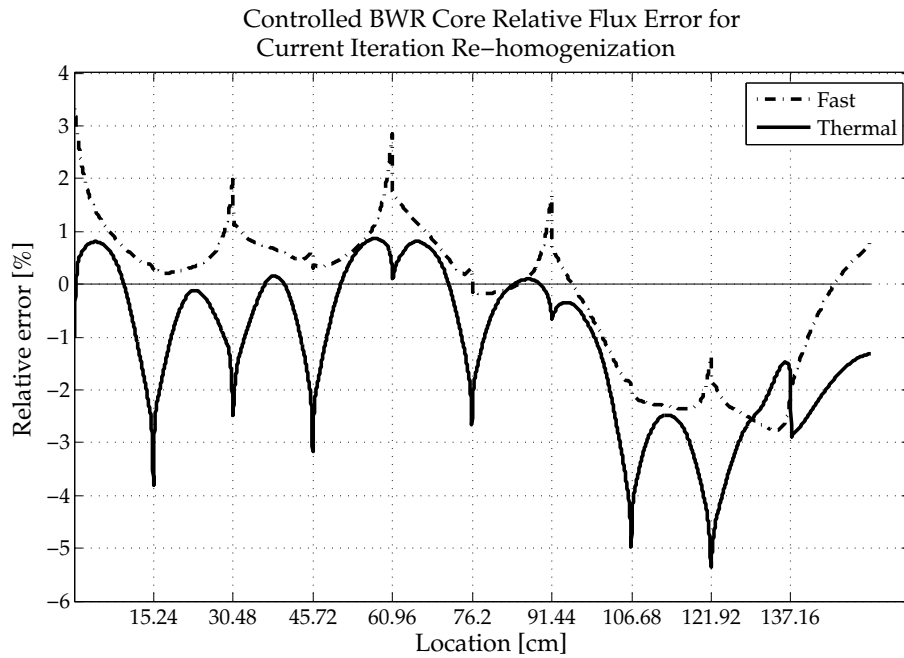
Figure 4: Relative flux error profile for the controlled BWR reactor with current iteration re-homogenization.

For comparison, Figures 8 and 9 plot the relative flux error when the problem is homogenized using discontinuity factors. The discontinuity factor calculations were performed using the same fine mesh as the heterogeneous problem in order to relax the dependence of the pre-assumed nodal shape[7]. As expected, diffusion theory with discontinuity factor homogenization does not effectively reproduce the transport solution. It should be noted that

16

Figure 5: Relative flux error profile for the controlled BWR reactor with diffusion approximation re-homogenization.
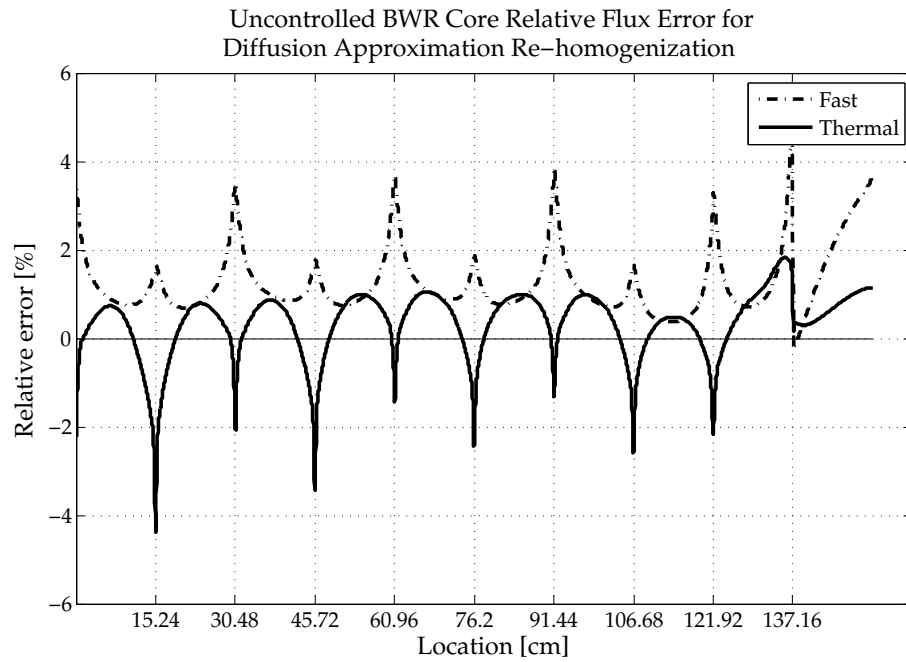
Figure 6: Relative flux error profile for the uncontrolled BWR reactor with diffusion approximation re-homogenization.
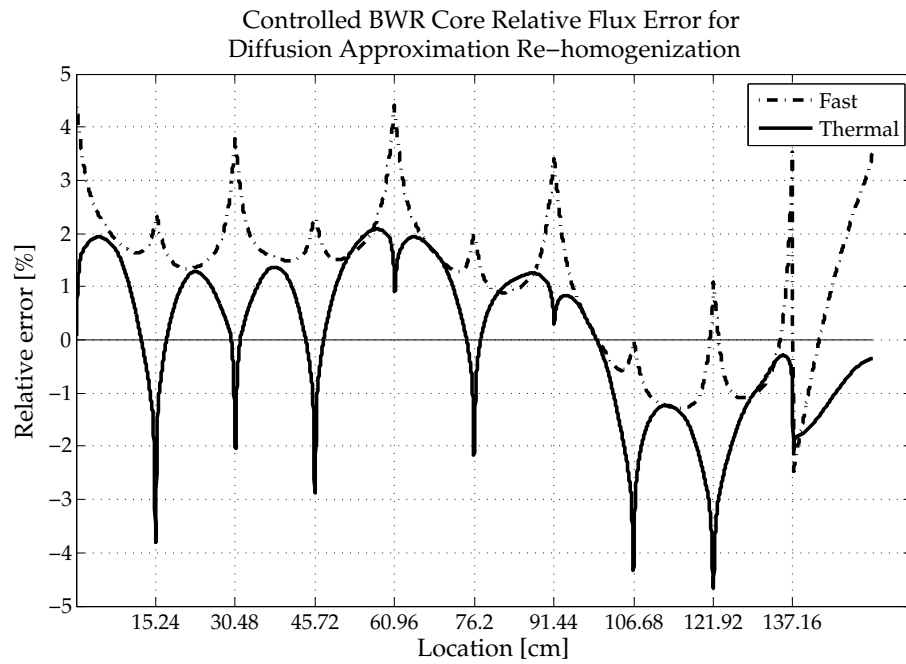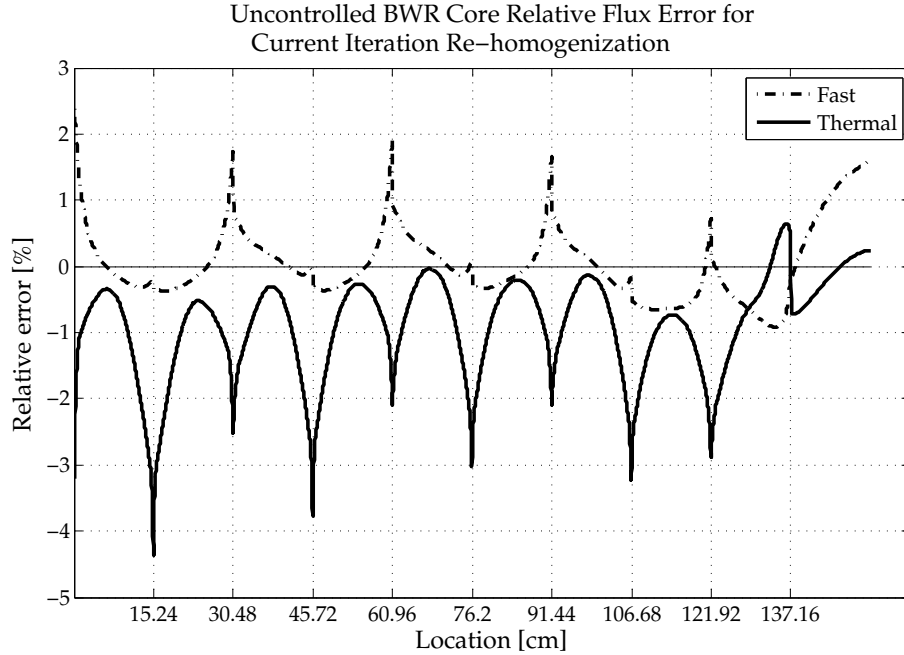
Figure 7: Relative flux error profile for the uncontrolled BWR reactor with current iteration re-homogenization.

the AVG error statistics are not the error in the average flux in each homogenized region, but point-by-point error averaged over the entire core. Discontinuity factor homogenizations are very accurate at reproducing the average flux in a homogenized region. This effect can be seen in how Figures 8 and 9 oscillate around the 0% line. On average the error is very close to zero. A tabulated summary of these results can be found in Table 6.

For additional comparison, Table 1 provides the results from each re-homogenization iteration of the CHSH homogenization and the results for discontinuity factor homogenization. For brevity, Table 1 only show the results for diffusion approximation based re-homogenization, as the results for current iteration re-homogenization are very similar. Note that the CHSH method achieves considerably smaller flux errors than the discontinuity factor method, even after just one iteration. However, it does not converge as accurately on the reactor eigenvalue in one iteration, requiring at least one re-homogenization to accurately calculate the eigenvalue.

Table 1: 1D BWR core results for each iteration of the CHSH method using Current Iteration re-homogenization compared with discontinuity factor errors

			AVG (%)		MAX (%)		MRE (%)	
	Iter.	Δk (pcm)	Fast	Thermal	Fast	Thermal	Fast	Thermal
ARO*	1	-365	2.4	2.4	7.0	11.7	2.0	2.2
	2	-8	1.4	0.9	6.5	4.5	1.2	0.8
	3	22	1.3	0.7	5.4	4.4	1.2	0.7
	4	24	1.3	0.7	5.5	4.4	1.2	0.7
SRI†	1	277	7.7	7.7	12.9	18.0	7.9	7.4
	2	64	1.4	1.1	4.4	5.4	1.5	1.2
	3	86	1.5	1.2	4.4	4.8	1.6	1.3
	4	86	1.5	1.2	4.4	4.7	1.6	1.3
ARO	DF‡	42	3.4	26.5	12.3	60.2	3.5	26.7
SRI	DF	146	3.2	22.8	12.7	57.5	3.3	23.4

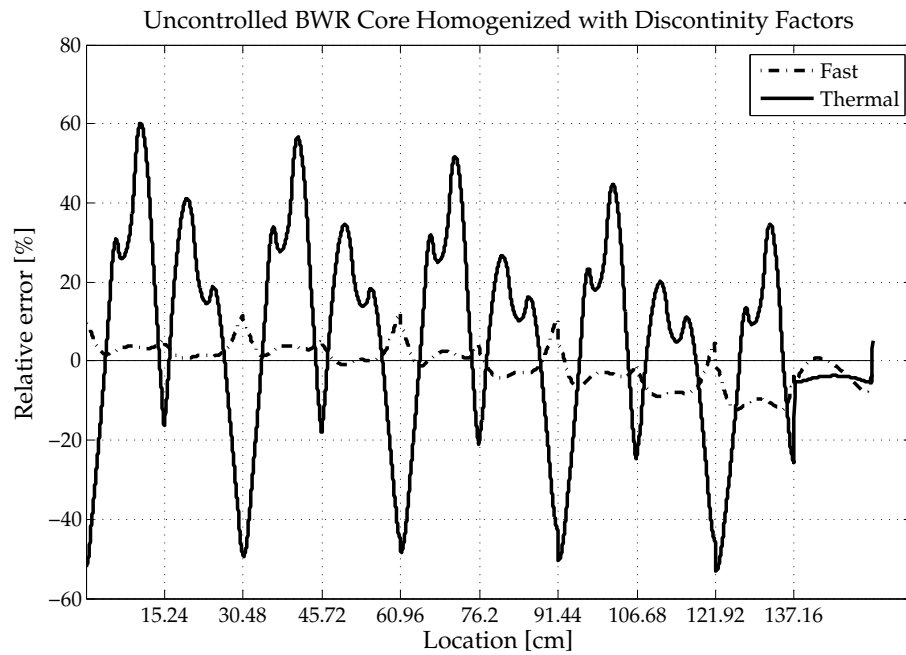*All rods out
†Some rods in
‡Discontinuity factor results

Figure 8: Relative flux error profile for the uncontrolled BWR reactor homogenized with discontinuity factors.
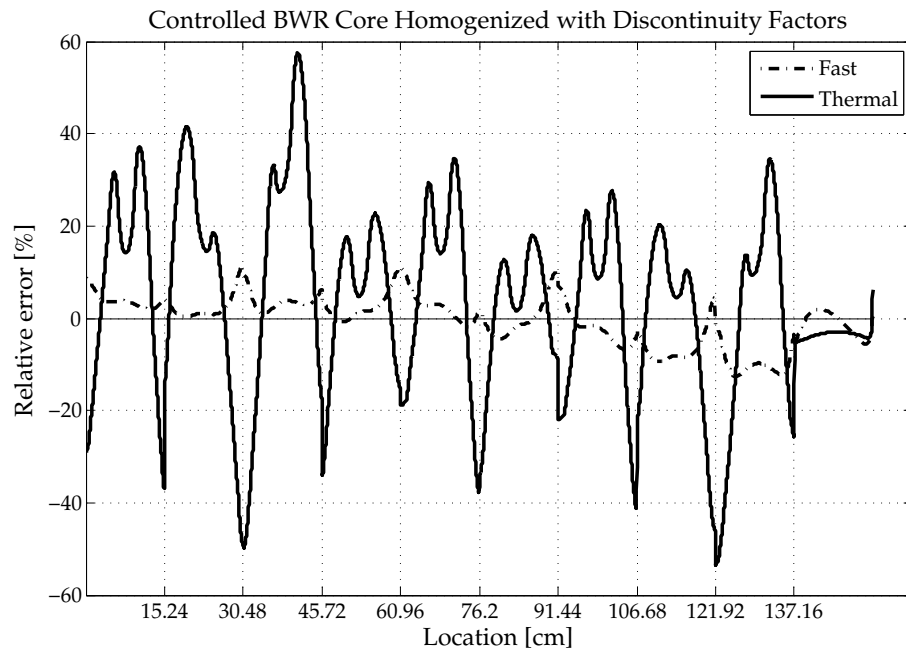

Figure 9: Relative flux error profile for the controlled BWR reactor homogenized with discontinuity factors.

4.1.2 1-D HTTR core

HTTR core calculations are performed on a 1-D benchmark problem based on a typical gas cooled prismatic block reactor core. The cross section library for this reactor were derived from a 2-D benchmark problem based on the Japanese High Temperature Test Reactor by Douglass and Rahnema[3]. A simple layout of the core can be found in Figure 10. The core consists of fifteen blocks and is modeled with center symmetry. There are total of six fuel blocks, four control blocks, and six reflector blocks in the reactor. Two configurations of this reactor are considered: one uncontrolled with all control rods out (ARO) and one controlled with all control rods in (ARI). The difference between the two configurations is that in the ARI configuration control rods have been inserted into the center control block, the outer control block, and the second fuel block.

The blocks of the reactor are highly heterogeneous. Each fuel block consists of six fuel pins and two graphite regions. The pins themselves are modeled as each having nine regions, including fuel, gas, sleeve, and graphite regions. Control blocks are modeled as two control rods with tube regions in a graphite block. For the ARI configuration, fuel block 2 has had number densities of control material smeared into its graphite regions, simulating the insertion of a control rod. The reactor has been modeled as specular reflective on the left side and with vacuum conditions on the right side.

The reference flux calculated for the controlled and uncontrolled HTTR cores can be found in Figures 11 and 12. The uncontrolled (ARO) configuration has a high eigenvalue of 1.10297, while the controlled (ARI) configuration has a low eigenvalue of 0.82959. The reference calculation is a fully heterogeneous 47 group S-8 calculation with half mean free path discretization, totaling about 900 total meshes for each reactor configuration. This is a coarser meshing than the BWR core due to the fact that the HTTR core is an optically thin reactor.

Figures 13 to 16 show the flux error results of the homogenized calculation on both core configurations and for the two different interface boundary condition approximations used in re-homogenization. All homogenized calculations were performed using a 47 group diffusion homogenized solver and a 47 group S-8 fixed-source assembly-level re-homogenization. Like
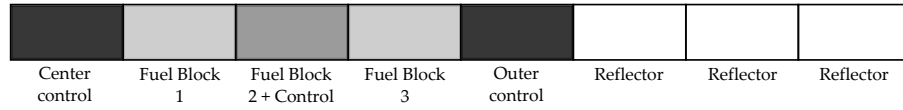
Figure 10: 1-D HTTR core layout. In the controlled configuration, control rod cross sections are used in fuel block 2 and in the outer control block.
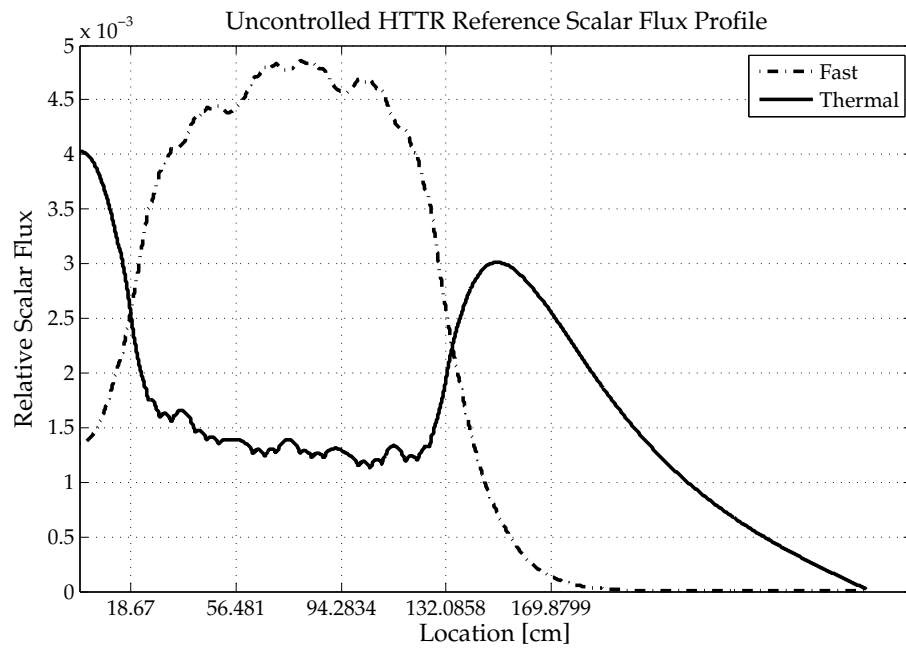

Figure 11: S-8 reference solution to the uncontrolled HTTR reactor, $k = 1.10297$. Vertical gridlines represent assembly interfaces.
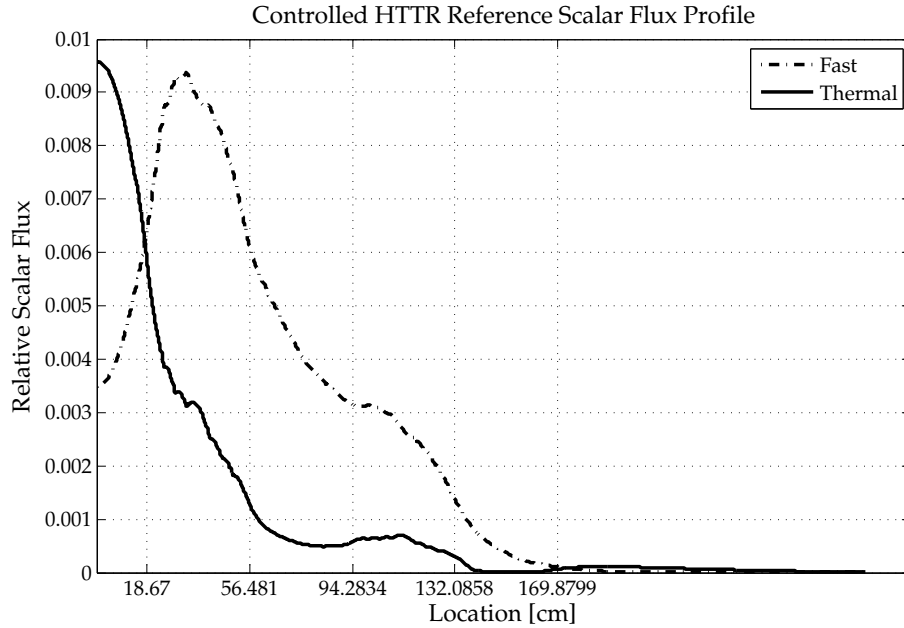
Figure 12: S-8 reference solution to the controlled HTTR reactor, $k = 0.82959$. Vertical gridlines represent assembly interfaces.

in the reference calculation, the core meshing for the homogenized case was taken to be about half of a mean free path for each core. This leads to a coarser mesh for the homogenized cores of about 400 total meshes. The HTTR cores tested both converged in six outer iterations to the same whole-core convergence criteria as used for the BWR cores. The extra two re-homogenization iterations are not unexpected, as the HTTR core has a significantly higher mean free path than the BWR core, meaning that the effects from neighboring blocks is more pronounced.

The plots of relative error given in Figures 13 to 16 have a very large error in the reflector region of the reactor for the fast flux. This is largely because of the extremely high anisotropy of fast flux in that region, and this error does not disappear with further iteration. However, this high max error – as high as 33% in the controlled reactor – can be overlooked for both reactors. Comparing against Figures 11 and 12, it can be seen that the fast flux in the reflector region is exceedingly low, so while the relative error is as high as 33% for those regions, the absolute flux error in those regions is nearly zero. Additionally, there is no fuel in the reflector region, so error in the reflector region does not translate to error in eigenvalue or in any

Figure 13: Relative flux error profile for the uncontrolled HTTR reactor with diffusion approximation re-homogenization.

Figure 14: Relative flux error profile for the uncontrolled HTTR reactor with current iteration re-homogenization.
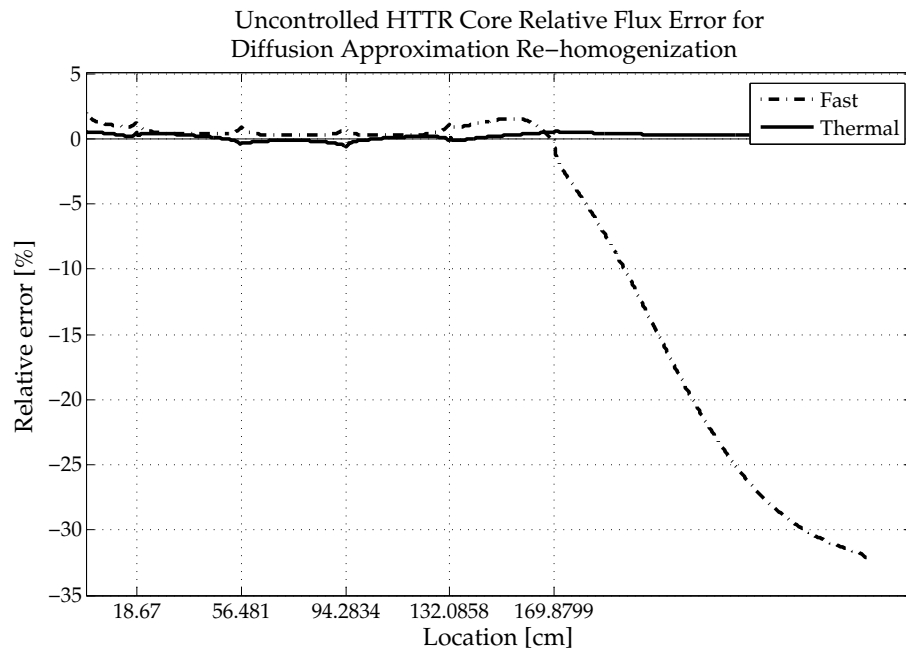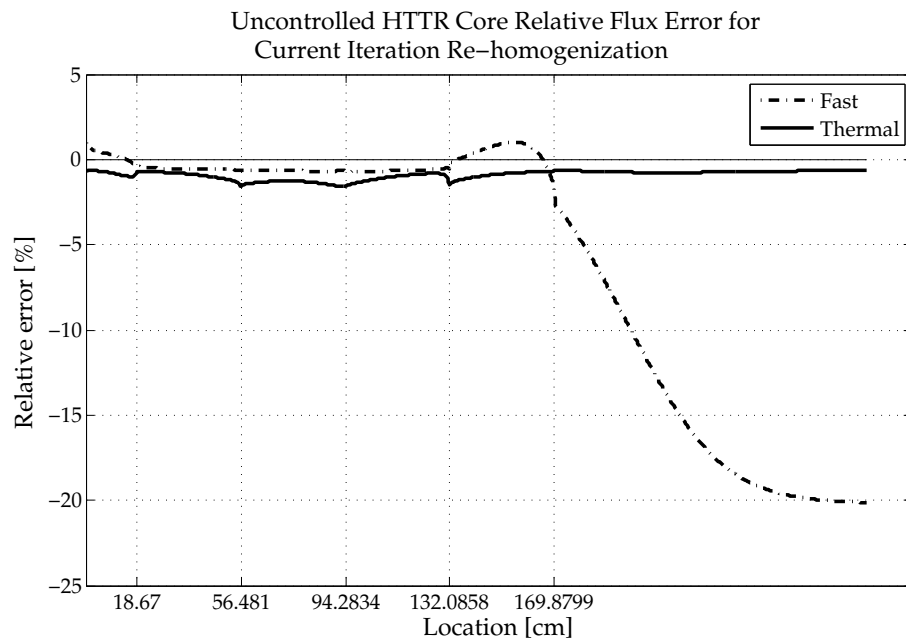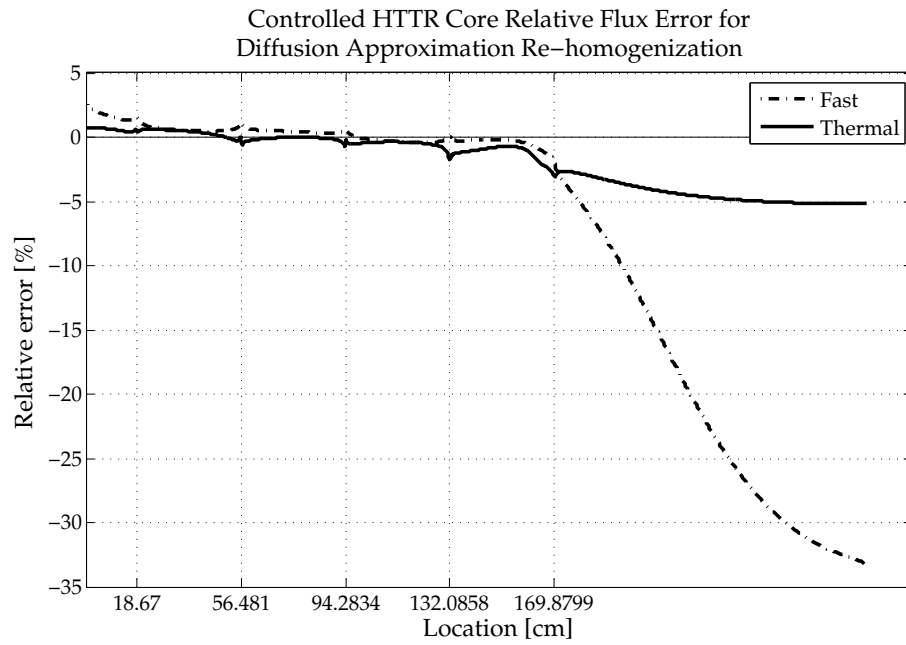
Figure 15: Relative flux error profile for the controlled HTTR reactor with diffusion approximation re-homogenization.
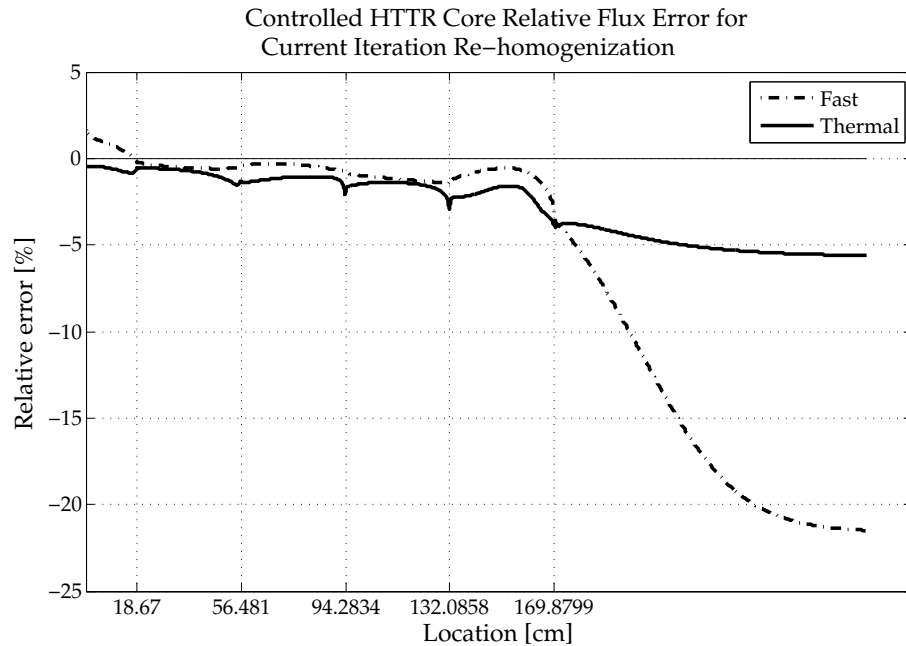
Figure 16: Relative flux error profile for the controlled HTTR reactor with current iteration re-homogenization.

reaction rates. For this reason, the mean relative error (MRE) column of Table 2 becomes very important, as it weights the error by the flux in each region. Observation of the MRE column indicates that the solution to both HTTR cases is within 1% of the reference flux at any point.

So that the flux error in the fuel regions can be discerned from the plots, Figures 17 to 20 provide the same information but truncate the reactor before the reflector region. In these plots it can be seen that, like the BWR cores, the HTTR cores have flux errors peaked at assembly interfaces for both re-homogenization methods. It can be seen that the current iteration re-homogenization tends to have significantly less peaking near assembly interfaces for the HTTR, especially in the fast groups, where there is virtually no peaking near assembly interfaces.
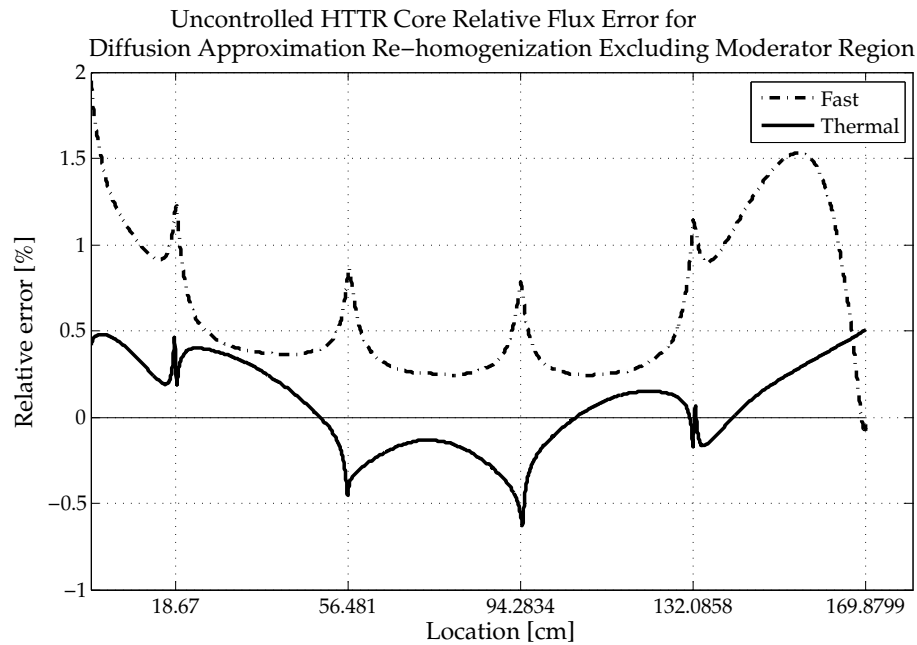
Figure 17: Relative flux error profile for the fuel and control regions of the uncontrolled HTTR reactor with diffusion approximation re-homogenization.

For comparison, the both configurations of the HTTR core have also been calculated using a discontinuity factor diffusion homogenization. The discontinuity factor homogenization does not work very well for the fast reactor due to high anisotropy throughout the reactor. Figures 21 and 22 show the flux error resulting from the discontinuity factor calculations. Note especially the effects of anisotropy in the controlled reactor, where the error reaches 80%
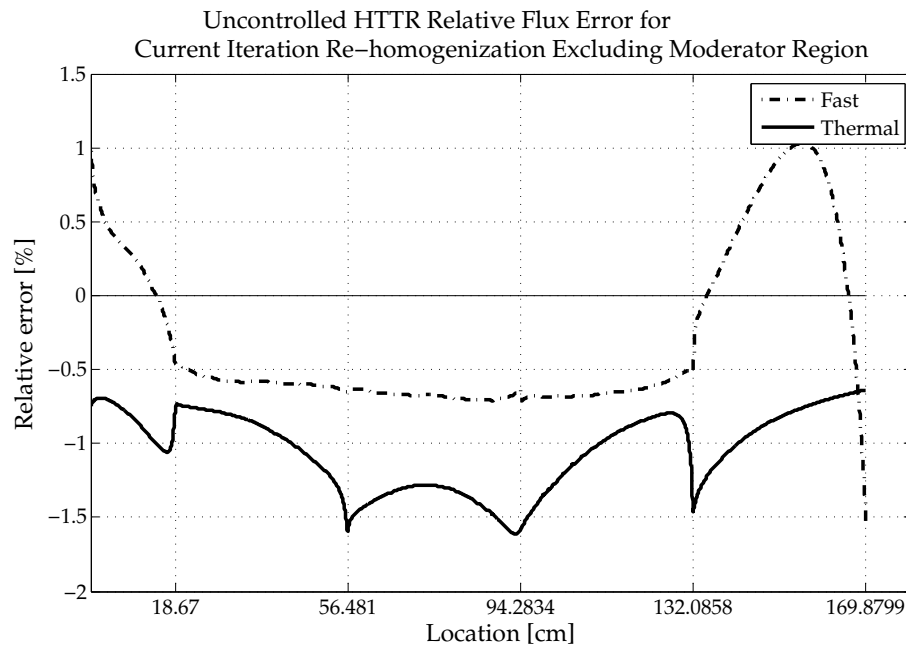
Figure 18: Relative flux error profile for the fuel and control regions of the uncontrolled HTTR reactor with current iteration re-homogenization.
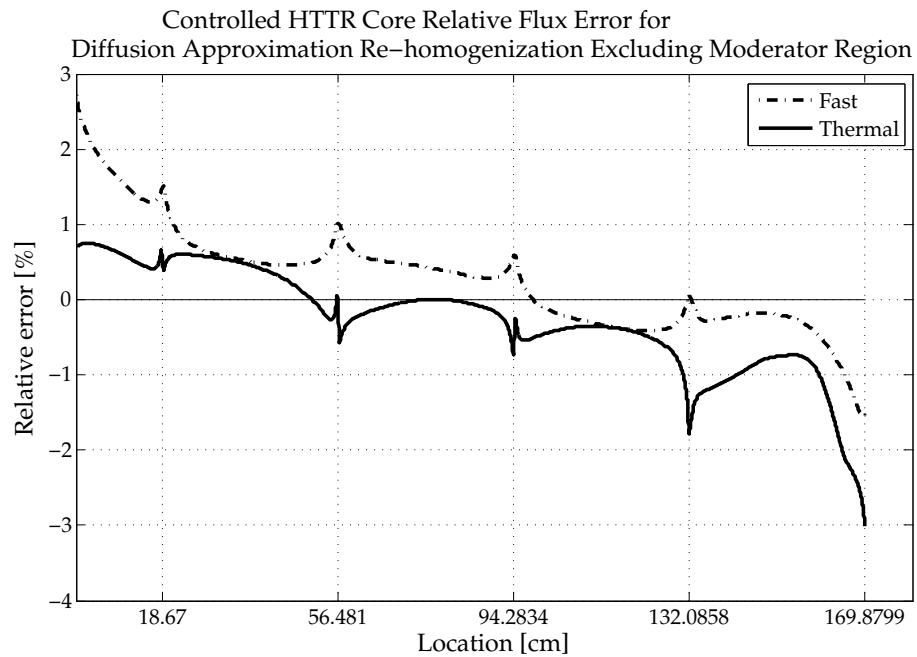
Figure 19: Relative flux error profile for the fuel and control regions of the controlled HTTR reactor with diffusion approximation re-homogenization.
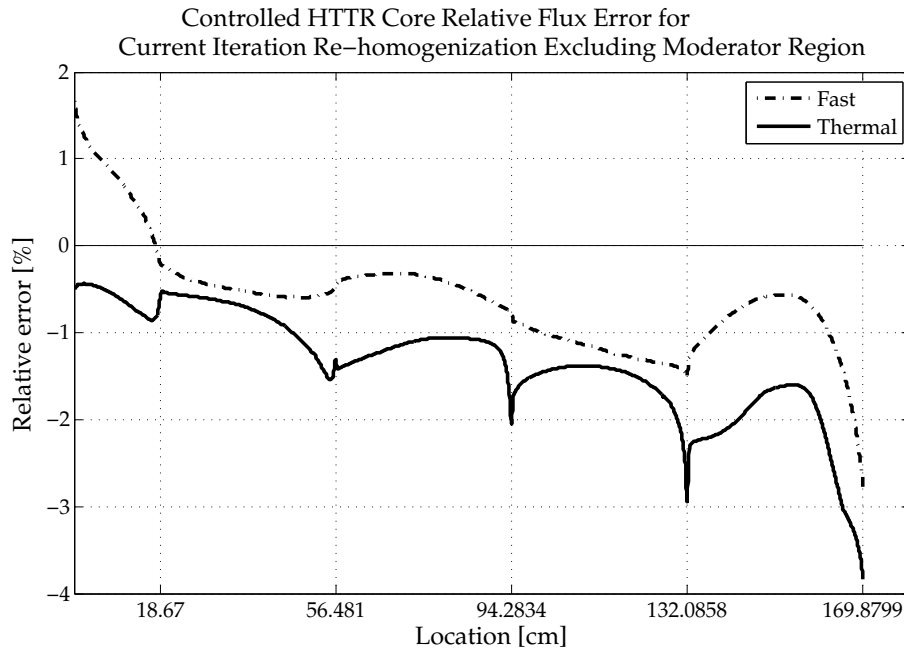
Figure 20: Relative flux error profile for the fuel and control regions of the controlled HTTR reactor with current iteration re-homogenization.

without oscillating back to 0%. In the BWR core, the the large flux errors of the discontinuity factor method averaged out over each bundle, resulting in an accurate approximation of the core eigenvalue. In the HTTR core, the error does not oscillate about 0%, so the error does not cancel in each homogenized region, which leads to high errors in eigenvalue. Table 2 is a breakdown of the CHSH results by iteration order. It can be seen that after one iteration the CHSH method obtains similar results to discontinuity factor methods, with slightly better flux errors and marginally more accurate eigenvalue results.
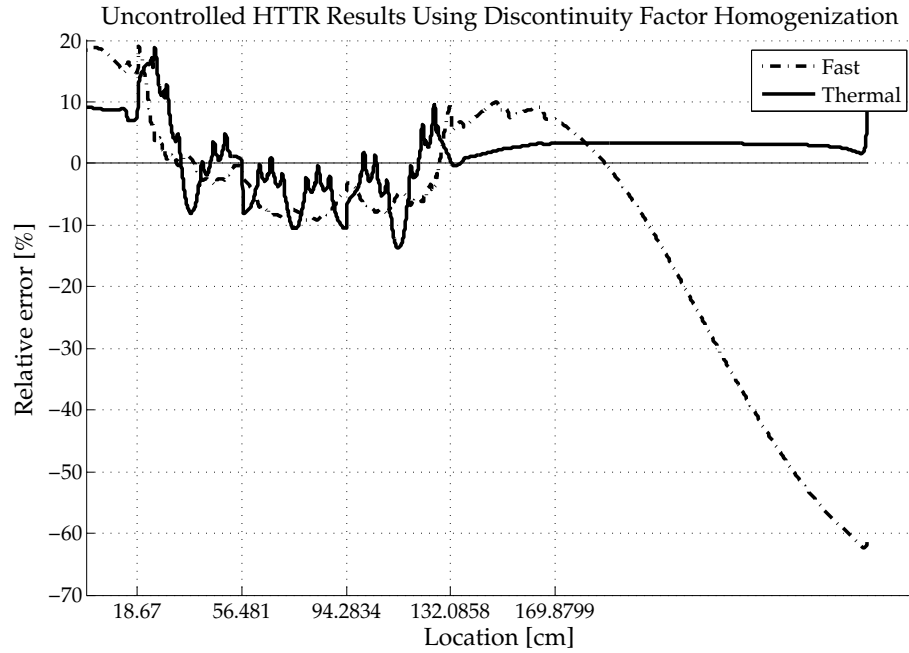
Figure 21: Relative flux error profile for the uncontrolled HTTR reactor with discontinuity factor homogenization.
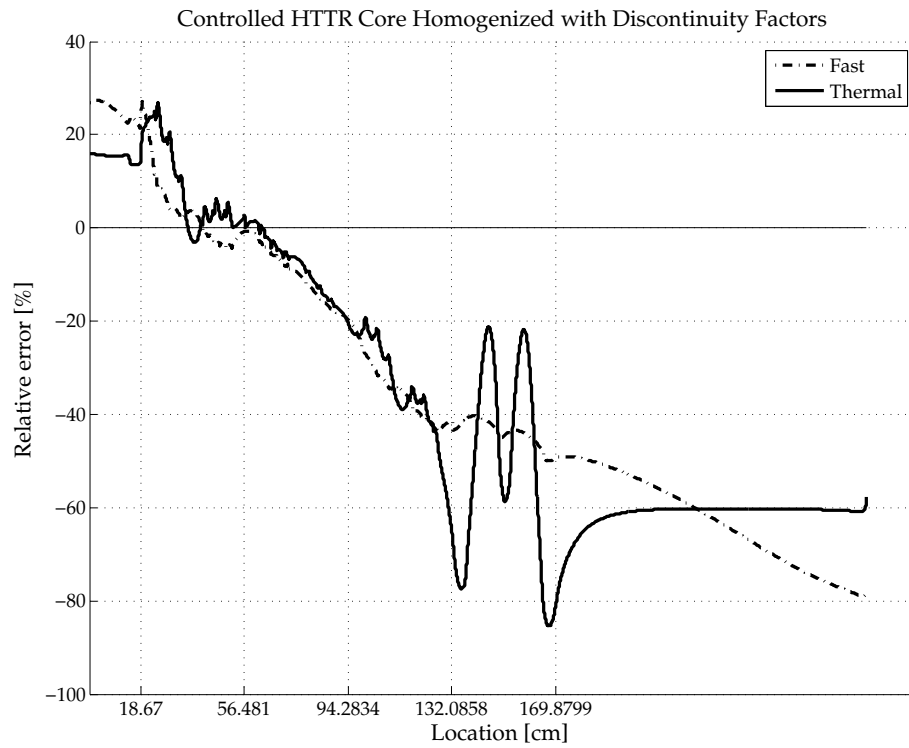
Figure 22: Relative flux error profile for the controlled HTTR reactor with discontinuity factor homogenization.

Table 2: 1D HTTR core results for each iteration of the CHSH method using Current Iteration re-homogenization compared with discontinuity factor errors

		Iter.	Δk (pcm)	AVG (%)		MAX (%)		MRE (%)	
				Fast	Thermal	Fast	Thermal	Fast	Thermal
ARO		1	-3510	9.9	3.3	29.9	9.4	5.0	3.7
		2	222	8.6	0.4	32.3	1.0	0.8	0.4
		3	-51	8.4	0.3	32.2	0.7	0.5	0.3
		4	-29	8.3	0.3	32.1	0.6	0.5	0.3
		5	-32	8.4	0.3	32.1	0.6	0.5	0.3
		6	-30	8.4	0.3	32.1	0.6	0.5	0.3
ARI		1	-6081	38.3	34.2	62.8	60.2	12.5	14.9
		2	584	7.9	3.4	28.1	7.6	1.3	1.1
		3	-95	8.9	2.1	33.6	5.0	0.7	0.7
		4	-18	8.6	2.1	33.3	5.1	0.7	0.6
		5	-29	8.6	2.1	33.3	5.2	0.7	0.6
		6	-27	8.6	2.1	33.3	5.2	0.7	0.6
ARO	DF		-3837	15.9	4.3	62.4	18.8	6.2	4.9
ARI	DF		-5560	39.4	39.5	79.1	85.4	12.4	15.8

4.2 Sources of error

For future improvements to the CHSH method it is important to examine the largest contributing factors to error in the solution. One of the most restrictive assumptions of the CHSH method is the method used to determine interface angular fluxes to use as boundary conditions for assembly-level fixed-source re-homogenization. This is restrictive because the diffusion homogenized solver is necessarily at most linearly anisotropic. The current iteration method of re-homogenization has been introduced to somewhat temper this effect, but it is interesting to examine the amount error to the solution that originates in the interface condition approximation.

To this end, this section presents a calculation wherein linearly anisotropic interface fluxes are calculated starting from the fine mesh heterogeneous reference solution. Those interface fluxes are then used as boundary conditions for assembly-level fixed-source calculations, and the results are compared to the reference solution. This manner of calculation assures that all of the error in the solution is introduced solely by the interface condition. Only the diffusion approximation interface approximation can be tested in this manner, due to the lack of an iteration on which to apply the current iteration method.

Figures 23 and 24 show the flux error introduced by the interface approximation for the controlled BWR core and the uncontrolled HTTR core. Like in the full CHSH method, the flux error is peaked at assembly interfaces, and peaks at similar values. Table 3 summarizes the results for all four core and configuration combinations. From this, it can be seen that the error introduced by the interface approximation comprises the vast majority of the error in the CHSH method, since the values in Table 3 are close to the full error in the CHSH method for both cores.
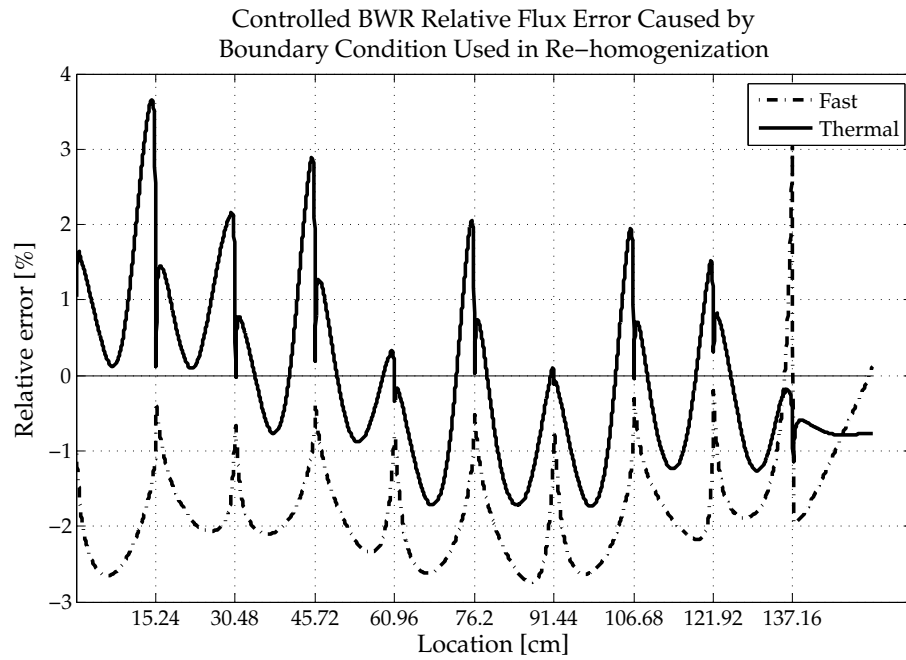
Figure 23: Relative flux error introduced by the interface boundary condition approximation for the 1-D controlled BWR core
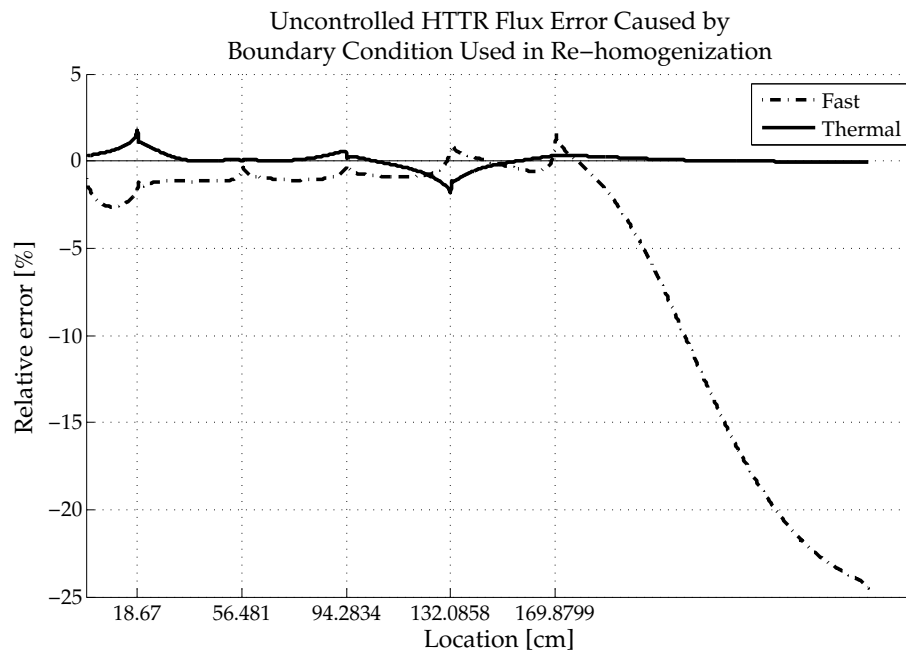
Figure 24: Relative flux error introduced by the interface boundary condition approximation for the 1-D uncontrolled HTTR core

Table 3: Flux errors resulting from performing fixed-source calculations using diffusion approximation boundary conditions generated from reference solutions.

		AVG (%)		MAX (%)		MRE (%)	
Core	Config.	Fast	Thermal	Fast	Thermal	Fast	Thermal
BWR	ARO	2.1	1.1	2.7	3.5	2.1	1.2
BWR	SRI	1.9	1.0	3.1	3.7	1.9	1.0
HTTR	ARO	5.4	0.9	24.3	2.3	0.7	0.7
HTTR	ARI	0.8	0.7	24.3	2.3	0.7	0.7

4.3   Computational efficiency analysis

Like in Yasseri and Rahnema's [13] discussion of the consistent spatial homogenization method, the CHSH method can benefit from progressively tightening convergence criteria. A progressively tightening convergence criteria is beneficial because the auxiliary cross section relies on the previous iteration's solution. The progressively tightening critera for the whole core calculation were initially set at $\epsilon_k = 10^{-5}$ and $\epsilon_\phi = 10^{-2}$, and then decreased by a factor of 10 for each iteration, to a minimum of $\epsilon_k = 10^{-8}$ and $\epsilon_\phi = 10^{-5}$. A different system of convergence criteria tightening or an adaptive system are not presented here, but could be expanded upon in future work.

Tables 4 and 5 summarize the complete results of the CHSH method without progressively tightening convergence. In particular, the column for Speedup displays the relative speed increase of the calculation to the reference calculation. Speedup is defined as $\frac{1}{\text{NCT}}$, where NCT is the Normalized Calculation Time, the calculation time normalized to the calculation time of the reference solution. Note that the HTTR cores actually take longer to calculate than the reference solution without progressively tightening convergence criteria. Tables 6 and 7 summarize the complete results with progressive convergence criteria. First, it should be noted that the progressive convergence criteria have virtually no effect on the solutions themselves, but serve purely to increase the speed of the calculation. For all cases, significant – and sometimes dramatic – improvement can be achieved by switching to progressive convergence criteria. With progressively tightening convergence criteria, the CHSH method converges between two and four times as fast as the reference solution, slower for optically thin cores, with at most 2% mean relative flux error.

Table 4: 1D BWR core computation time comparison for two different re-homogenization schemes with fixed convergence criteria

				AVG (%)		MAX (%)		MRE (%)	
		Speedup[§]	Δk (pcm)	Fast	Thermal	Fast	Thermal	Fast	Thermal
ARO	DA[¶]	2.25	24	1.2	0.7	5.5	4.4	1.2	0.7
	CI[‖]	2.72	86	2.0	1.1	4.4	4.7	2.0	1.0
SRI	DA	2.72	86	2.0	1.1	4.4	4.7	2.0	1.0
	CI	2.67	90	0.8	0.8	3.3	5.3	0.8	0.9
ARO	DF		42	3.4	26.5	12.3	60.2	3.5	26.7
SRI	DF		146	3.2	22.8	12.7	57.5	3.3	23.4

Table 5: 1D HTTR core computation time comparison for two different re-homogenization schemes with fixed convergence criteria

				AVG (%)		MAX (%)		MRE (%)	
		Speedup	Δk (pcm)	Fast	Thermal	Fast	Thermal	Fast	Thermal
ARO	DA	1.23	-30	8.4	0.3	32.1	0.6	0.5	0.3
	CI	0.98	-27	6.2	0.9	20.1	1.6	0.6	0.9
ARI	DA	0.94	-27	8.6	2.1	33.3	5.2	0.7	0.6
	CI	0.84	-17	6.6	2.8	21.5	5.6	0.6	0.8
ARO	DF		-3837	15.9	4.3	62.4	18.8	6.2	4.9
ARI	DF		-5560	39.4	39.5	79.1	85.4	12.4	15.8

[§]$\frac{1}{\text{NCT}}$, where NCT is Normalized computation time (normalized to the reference calculation)
[¶]Diffusion approximation re-homogenization conditions
[‖]Current iteration re-homogenization conditions

Table 6: 1D BWR core computation time comparison for two different re-homogenization schemes with progressively tightening convergence criteria

		Speedup	Δk (pcm)	AVG (%) Fast	AVG (%) Thermal	MAX (%) Fast	MAX (%) Thermal	MRE (%) Fast	MRE (%) Thermal
ARO	DA	2.72	24	1.3	0.7	5.3	4.3	1.3	0.7
	CI	3.12	29	0.4	1.0	2.5	4.1	0.4	1.0
SRI	DA	3.52	85	2.0	1.1	4.4	4.7	2.0	1.0
	CI	4.29	89	0.9	0.8	3.4	5.4	0.9	0.9
ARO	DF		42	3.4	26.5	12.3	60.2	3.5	26.7
SRI	DF		146	3.2	22.8	12.7	57.5	3.3	23.4

Table 7: 1D HTTR core computation time comparison for two different re-homogenization schemes with progressively tightening convergence criteria

		Speedup	Δk (pcm)	AVG (%) Fast	AVG (%) Thermal	MAX (%) Fast	MAX (%) Thermal	MRE (%) Fast	MRE (%) Thermal
ARO	DA	2.72	-26	8.4	0.3	32.2	0.6	0.5	0.3
	CI	2.89	-24	6.2	0.9	20.1	1.6	0.6	0.9
ARI	DA	1.98	-25	8.6	1.9	33.3	4.6	0.7	0.6
	CI	1.84	-16	6.6	2.6	21.5	5.0	0.6	0.8
ARO	DF		-3837	15.9	4.3	62.4	18.8	6.2	4.9
ARI	DF		-5560	39.4	39.5	79.1	85.4	12.4	15.8

CHAPTER V

CONCLUDING REMARKS AND FUTURE WORK

In this work, a consistent hybrid diffusion-transport spatial homogenization (CHSH) method has been developed that makes use of conventional flux-weighted cross sections and reproduces the heterogeneous transport solution to mean relative error of 2% with 2 to 4 times faster computational speed. The method solves the whole-core calculation using homogenized diffusion theory and then makes use of on-the-fly transport re-homogenization to update its auxiliary source term.

The CHSH method has been verified for stylized BWR and HTTR benchmark problems in 1-D configurations. Two different approximations were tested for the boundary conditions used in re-homogenization. The first, the diffusion approximation (DA) method uses the diffusion solution to develop a linearly anisotropic flux at assembly interfaces. The second, the current iteration (CI) weights the previous iteration's transport-calculated interface flux with the change in incoming current at the boundary. The DA method is sufficient in thermal reactors, but for the fast reactor the CI method has better accuracy. Additionally, the fast reactor required six re-homogenization iterations to converge, while the BWR required only four.

It was shown that most of the error introduced by the CHSH homogenization comes from the approximation used as the interface condition, and so for future work other re-homogenization methods should be considered. One method which has shown promise in preliminary testing is to perform a single core sweep during re-homogenization instead of assembly-level fixed-source calculations altogether. This method may also save significant computational time, as the assembly-level fixed-source calculations require many iterations to converge.

Another interesting area of potential future work involves simultaneously collapsing energy groups while homogenizing in space. As presented, the CHSH method does not involve

any collapsing in energy, but does not prohibit simultaneous collapsing. Simultaneous collapse of the energy variable could greatly increase computational efficiency to make this method more practical.

REFERENCES

[1] ANISTRATOV, D., "Consistent spatial approximation of the low-order quasi-diffusion equations on coarse grids," *Nucl. Sci. & Eng.*, vol. 149, pp. 138–161, 2005.

[2] DOUGLASS, S. and RAHNEMA, F., "Development of a 1-D boiling water reactor benchmark specification," *Trans. Am. Nucl. Soc.*, vol. 102, pp. 543–545, June 2010.

[3] DOUGLASS, S. and RAHNEMA, F., "Specification for a 1-dimensional gas-cooled reactor benchmark problem for neutron transport," *Trans. Am. Nucl. Soc.*, vol. 102, pp. 74–78, May 2010.

[4] HIRUTA, H. and ANISTRATOV, D., "Homogenization method for the two-dimensional low-order quasi-diffusion equations for reactor core calculations," *Nucl. Sci. & Eng.*, vol. 154, pp. 328–352, 2006.

[5] KELLEY, D., "Depletion of a BWR lattice using RACER continuous energy monte carlo code," in *Proc. Int. Conf. Mathematics and Computations, Reactor Physics and Environmental Analyses*, vol. 2, p. 1011, American Nuclear Society, April 1995.

[6] KOZLOWSKI, T., XU, Y., DOWNAR, T., and LEE, "Cell homogenization method for pin-by-pin neutron transport calculations," *Nucl. Sci. & Eng.*, vol. 82, pp. 1–18, 2011.

[7] RAHNEMA, F. and MCKINLEY, M., "High-order cross-section homogenization method," *Annals of Nuclear Energy*, vol. 29, pp. 875–899, 2002.

[8] RAO, J. V. M. and LEE, S. M., "Analysis of homogenization methods for neutron transport in lattices," *Nucl. Sci. & Eng.*, vol. 82, pp. 71–77, 1982.

[9] ROBERTS, D., OUISLOUMEN, M., KUCUKBOYACI, V., and IVANOV, K., "Development of iterative transport-diffusion methodology for LWR analysis," in *Advances in Reactor Physics to Power Nuclear Renaissance*, (Pittsburgh, PA), PHYSOR, 2010.

[10] SANCHEZ, R., "Assembly homogenization techniques for core calculations," *Progress in Nuclear Energy*, vol. 51, pp. 14–31, 2009.

[11] SIMEONOV, T., *Release Notes for Helios System 1.8*. Studsvik Scandpower Report, 26 November 2003.

[12] SMITH, K., "Assembly homogenization techniques for light water reactor analysis," *Progress in Nuclear Energy*, vol. 17, no. 3, pp. 303–335, 1986.

[13] YASSERI, S. and RAHNEMA, F., "Consistent spatial homogenization in transport theory," *Nucl. Sci. Eng.*, December 2013. Accepted.